Available online at www.sciencedirect.com

ScienceDirect

journal homepage: www.elsevier.com/locate/he

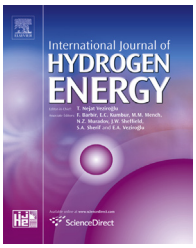

Synchrotron-based structural and spectroscopic studies of ball milled RuSeMo and RuSnMo particles as oxygen reduction electrocatalyst for PEM fuel cells

K. Suarez-Alcantara [a,b,*], A. Ezeta-Mejia [c], M. Ortega-Avilés [d], D. Haase [e], E. Arce-Estrada [c], R.G. Gonzalez-Huerta [c], O. Solorza-Feria [f], S.E. Canton [a]

[a] Department of Synchrotron Radiation Instrumentation, Lund University, Ole Römers väg 1, SE-22363 Lund, Sweden
[b] UNAM-IIM Morelia, Antigua carretera a Pátzcuaro 8710, Col. Ex-hacienda de San José de la Huerta, Morelia, Michoacán 58190, Mexico
[c] Superior School of Chemical Engineering and Extractive Industries (ESIQIE) of National Polytechnic Institute, UPALM Ed. 7, 07738 Zacatenco, México DF, Mexico
[d] Nanoscience, Micro and Nanotechnology Center of National Polytechnic Institute, Luis Enrique Erro s/n, 07738 Zacatenco, México DF, Mexico
[e] MAX IV Laboratory, Lund University, Ole Römers väg 1, SE-22363 Lund, Sweden
[f] Center of Research and Advanced Studies (CINVESTAV), A. Postal 14-740, 07360 México DF, Mexico

ARTICLE INFO

Article history:
Received 1 December 2013
Received in revised form
27 March 2014
Accepted 29 March 2014
Available online 3 May 2014

Keywords:
Ruthenium particles
Electrocatalyst
Fuel cells
Synchrotron radiation

ABSTRACT

Particles of RuSeMo and RuSnMo have been produced by ball milling; they present catalytic activity towards the oxygen reduction reaction (ORR) in acid media. A Tafel slope close to 120 mV/dec was found for both materials. Their morphology was first characterized by scanning electron microscopy (SEM) and transmission electron microscopy (TEM). SEM and TEM images reveal particles in the sub-micrometer range. The structure of the materials was further probed with synchrotron radiation powder X-ray diffraction (SR-PXD) and X-ray absorption spectroscopy (XAS). SR-PXD reveals the existence of metallic Ru as the main phase and the formation of phases such as $RuSe_2$ in RuSeMo and Ru_3Sn_7 in RuSnMo. Mo was found to form solid solution into the $RuSe_2$ phase in ball milled RuSeMo. Finally, The Ru L_3-edge and Mo L_3-edge XAS fingerprints were correlated with the catalytic activity towards ORR.

* *Corresponding author*. UNAM-IIM Morelia, Antigua carretera a Pátzcuaro 8710, Col. Ex-hacienda de San José de la Huerta, Morelia, Michoacán 58190, Mexico. Tel.: +52 4433222777.
E-mail address: karina_suarez@iim.unam.mx (K. Suarez-Alcantara).
http://dx.doi.org/10.1016/j.ijhydene.2014.03.220

Introduction

Polymer electrolyte membrane fuel cells (PEMFCs) are considered potential alternatives to the conventional internal combustion engine in automobile applications [1]. However, several shortcomings still limit their commercialization on a large scale. One crucial issue is the cost and limited availability of the Pt necessary as fuel cell electrocatalyst. The efforts to reduce the amount of Pt in electrocatalysts for fuel cells include: 1) the use of suitable supporting materials; 2) the formation of Pt alloys with non-noble metals, and 3) alternative electrocatalysts without any Pt. Electrocatalysts for low temperature PEMFCs are extensively studied with the aim of improving their catalytic activity, selectivity and stability. Ru based electrocatalysts are well known because of their relatively high activity towards the oxygen reduction reaction (ORR), high tolerance to CO poisoning and stability in acid media [2,3] that can be attractive to specific applications. It is recognized that the activity towards ORR of Ru-electrocatalysts is enhanced by the incorporation of Se [4]. The addition of a second transition metal, *i.e.* Mo, Cr, W or Fe, to the Ru–Se particles increases the ORR activity further [5–7]. Typically the Ru–Se and Ru–Mo–Se electrocatalysts have been produced by thermolysis of $Ru_3(CO)_{12}$ and $Mo(CO)_6$ in a suitable solvent (*i.e.* xylene or 1,6-hexanediol). The solvated carbonyl precursors are decarboxylated and the products co-precipitate with Se to form chalcogenides [4,7]. A relatively unexplored method to produce electrocatalytic alloys for fuel cell is the mechanical milling or ball milling [8,9]. Ball milling is a high energy, quick synthesis procedure that can be easily up-scaled. Ball milling has the advantage of eliminating the solvents during the synthesis, washing and purification of materials; but can produce a complicated mixture of metastable or disordered phases [10,11]. As a relatively new synthesis procedure for fuel cell purposes, the products and byproducts of ball milling must be characterized in detail. Synchrotron radiation is an extremely intense beam that allows fast imaging, scattering, diffraction or X-ray absorption studies. These techniques can make an important contribution to electrocatalysts characterization [12]. In the present work ball milled RuSeMo and RuSnMo particles were studied in detail by the synchrotron radiation powder X-ray diffraction (SR-PXD) and X-ray absorption spectroscopy (XAS). Despite their importance as electrocatalyst or catalyst (not limited to hydrogen/oxygen fuel cells), experiments at the Ru and Mo L_3-edges are not comprehensively available in the open literature. XAS at the L-edges can provide direct and valuable information on the *d*-electron density of the metal center. This is of paramount importance for an ORR electrocatalyst, because of the well known relationship between the *d*-band occupancy/vacancy and the catalyst activity [13].

Experimental description

The syntheses procedure of the ball milled Ru based particles is described elsewhere [14,15]. Briefly, powder precursors (Ru, Se, Sn and Sn Aldrich, 99.9% nominal purity) in an atomic ratio 2:1:1 (2 at Ru) were milled in a high energy ball mill SPEX 8000 for 40 h. Steel vial and zirconia balls were used for producing RuSeMo and RuSnMo. The ball to powder ratio was 4:1 and methanol was used as process control agent. The milling vial was sealed under argon atmosphere. The as-milled powders were characterized without further treatment.

Electrochemistry measurements of rotating disk electrode (RDE) were taken in a conventional three electrode arrangement [14,15]. Each electrocatalytic powder was mixed with Nafion® monomer and ethanol to form a suspension or "ink": 1 mg electrocatalyst, 0.4 mg of Vulcan, 12 μl of Nafion® monomer and 0.3 ml of ethanol. A glassy carbon electrode (5 mm diameter) was coated with 5 μl the suspension and dried at room temperature. This thin-film electrode arrangement was the working electrode. A platinum wire was the counter electrode and a saturated Calomel electrode (SCE) was the reference electrode. The electrolyte (H_2SO_4, 0.5 M) was oxygen saturated before each measurement. The rotation of the working electrode was varied from 100 to 1600 rpm. Kinetic current density was obtained by appropriated mass transfer effects correction according with Koutecky-Levich first order reaction approach [14–16]. Once the kinetic current was extracted; the j_k versus *E* data was plotted in the typical fuel cell performance style. The resistance losses were extracted from the slope of the linear region of the j_k versus *E* plot.

Scanning electron microscopy (SEM) micrographs were taken with secondary electrons at a Quanta 3D FEG scanning electron microscope. The samples were dispersed ultrasonically in ethanol and then one drop was deposited on extra-smooth graphite tape. Transmission electron microscopy (TEM) micrographs were taken at 300 kV at Tecnai G2 F30 from FEI microscope. The samples were dispersed in isopropyl alcohol, the dispersion was ultra-sonicated 6 times in periods of 5 min in the ultrasonic bath with a 2 h resting time; then one drop was deposited on a copper sample holder. Energy-dispersive X-ray spectroscopy (EDS) was used as a quick method to determine the presence of the starting ball milled elements and possible contamination from vial or balls.

All synchrotron radiation experiments were performed at the MAX-lab facility, Sweden. Synchrotron radiation Powder X-ray diffraction (SR-PXD) patterns were taken at the I711 beamline. The samples were sealed in glass capillaries (0.3 mm diameter). The wavelength was 1.0085 Å. A CCD detector (Titan CCD camera) was used to collect data. Exposure time of 240 s and appropriate rotation of capillary was set [17]. Radial integration was performed with the fit2d software [18].

X-ray Absorption (XAS) experiments were accomplished at the Ru L_3-edge and Mo L_3-edge at the I811 beamline. 1 mg of each powder sample was finely dispersed on 1.5 cm^2 of the glue-side of Kapton® tape and placed inside a He-filled cell. XAS experiments were performed in Fluorescence mode. Samples were oriented at 45° with respect the incident beam. 3 scans were measured and averaged. No indication of sample damage was observed. Data extraction was executed with Athena program [19]. No further correction for self-absorption effects was made.

Results and discussion

Detailed electrochemical characterization by means of cyclic voltammetry (CV) and rotating disc electrode (RDE) in acid

Table 1 – Kinetic parameter of ORR at 25 °C, composition.

Material	Synthetic procedure	Open circuit potential [V versus NHE]	Tafel slope at 25 °C [mV/dec]	j_0 at 25 °C [mA cm^{-2}]	Resistance loss [Ω cm^2]	EDS elemental composition analysis and edge [atomic%]	Composition (Rietveld method) [wt.%]	Composition from Rietveld method [atomic%]
RuSeMo	Ball milling	0.81 [15]	121.5 [15]	6.8×10^{-6} [15]	256.0	Ru(K): 75.5 ± 0.6 Se(K): 19.0 ± 0.6 Mo(K): 5.5 ± 0.3	Ru: 65.9 ± 1.0 $RuSe_2$: 33.2 ± 0.9 Mo: 0.8 ± 1.0	Ru: 74.8 Se: 24.4 Mo: 0.8
RuSnMo	Ball milling	0.71 [15]	110.6 [15]	1.3×10^{-6} [15]	206.0	Ru(K): 51.3 ± 0.6 Sn(K): 17.4 ± 0.5 Mo(K): 31.3 ± 0.4	Ru: 60.7 ± 1.0 Mo: 18.7 ± 1.0 Ru_3Sn_7: 20.6 ± 0.8	Ru: 67.0 Sn: 13.0 Mo: 20.0
$Ru_xMo_ySe_z$ [21]	Thermolysis of carbonyl precursors in 1,6-hexanediol	0.86	116.0	4.82×10^{-5}	20.0	$Ru_6Mo_1Se_3$	–	–

media can be found elsewhere [15]. Table 1 collects the electrochemical relevant data for correlation with XAS findings. Briefly, the Tafel slope near 120 mV/dec and the number of electrons transferred $n = 4e^-$ in both materials are associated to the water formation. These values have been used to propose the ORR mechanism. A common accepted ORR mechanism in acid media involves the competition between the dissociative adsorption (eq. (1)) versus the reductive adsorption of oxygen (eq. (3)) [20]; *i.e.* the coverage of O versus OH species over the electrocatalyst surface:

$$\frac{1}{2}O_2 \leftrightarrow O_{ad} \quad \text{Dissociative adsorption} \quad \text{Tafel slope} = 60\ \text{mV/dec} \tag{1}$$

$$O_{ad} + H^+ + e^- \leftrightarrow OH_{ad} \quad \text{Reductive transition} \tag{2}$$

$$\frac{1}{2}O_2 + H^+ + e^- \leftrightarrow OH_{ad} \quad \text{Reductive adsorption} \quad \text{Tafel slope} = 120\ \text{mV/dec} \tag{3}$$

$$OH_{ad} + H^+ + e^- \leftrightarrow H_2O \quad \text{Reductive desorption} \tag{4}$$

The Tafel slope depends on the coverage of O versus OH, which in turn depends on the electrode material and potential. In acid media, the OH coverage is related to a Tafel slope of 120 mV/dec; while the O coverage is related to 60 mV/dec [20]. The Tafel slope value of 120 mV/dec at both studied materials is characteristic of Ru based electrocatalyst in acid media. Based on this model, the ORR mechanism over this Ru-electrocatalysts is ruled by the OH coverage at low overpotential.

The electrocatalytic activity (estimated as the exchange current density j_0 *i.e.* the extrapolated kinetic current density at zero overpotential), is affected by the presence of Se or Sn: a decrease of 50 mV in the open circuit potential (OPC) in ball milled RuSnMo drives the exchange current density to lower values. The exchange current density values are collected in Table 1, their order of magnitude is such that: RuSeMo > RuSnMo. Exchange current density values of 10^{-6} mA cm^{-2} are low compared to the values obtained in similar carbon supported materials synthesized by thermolysis of carbonyl precursors, where values of 10^{-5} mA cm^{-2} at room temperature are the common [7,21]. However as an alternative synthetic route, the ball milled products must be characterized in detail.

Despite that the electrochemical kinetic data OCP, Tafel slope and exchange current density in Table 1 describe the ball milled RuSeMo as better electrocatalyst than ball milled RuSnMo; peculiar observations at the kinetic current density versus potential must be stated. The RDE complete set of curves reported elsewhere [15] presented low definition of the mixed and diffusional potential zones and high overpotential for the ORR (inset of Fig. 1, RDE polarization curves taken at 1600 rpm). For comparison purposes our old $Ru_xMo_ySe_z$ synthesized by thermolysis of carbonyl precursors [21] was analyzed in the same way as the ball milled materials. The high overpotential for the ORR al ball milled materials can be attributed to ohmic losses. However from RDE curves it is not easy to visualize or to extract the resistance losses. Fig. 1 presents the corrected kinetic current density versus potential in acid medium of RuSeMo and RuSnMo extracted from RDE curves [15,21] plotted in a typical fuel cell performance style [22]. From that figure, the high ohmic drops are easy to visualize and estimate. The resistance losses are 256 Ω cm^2 for RuSeMo and 206 Ω cm^2 for RuSnMo; these values are referred

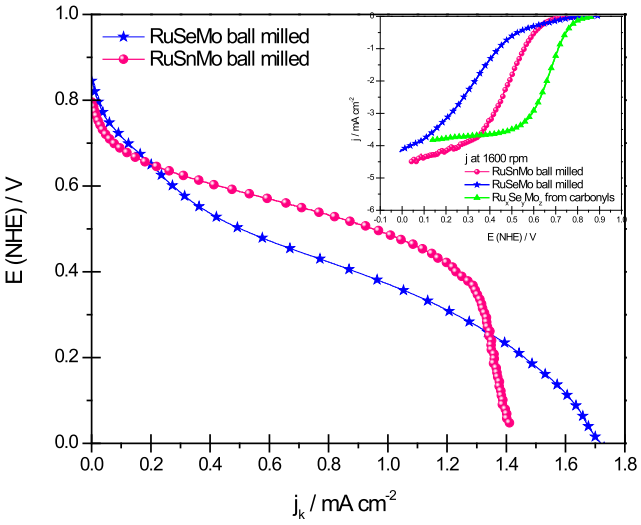

Fig. 1 – Kinetic current density–potential curves of ball milled RuSeMo and RuSnMo. Inset RDE curves at 1600 rpm of ball milled RuMoSe [15] and RuMoSn [15] and Ru_xMo_ySez synthesized from carbonyls [21] in 0.5 M H_2SO_4 at 25 °C.

to the electrode geometrical area. Notwithstanding that the Tafel slope and the OCP are quite similar; the ohmic resistance at $Ru_xMo_ySe_z$ from carbonyls is 20.0 Ω cm^2. The ohmic resistance, overpotential and electrochemical activity are closely related. The characterization below can help explaining the relationship.

Fig. 2 displays the SEM images of the studied materials. It is well known that the ball milling of Ru-electrocatalyst family produces micrometer aggregates about 10–30 μm [14,15]. Fig. 2(a) and (b) present the RuSeMo and RuSnMo SEM, the ultrasonic treatment divided the large aggregates into small aggregates well below 1 μm in size; with irregular aggregate morphology but spherical-like particles. To allow more detailed images, TEM was performed. The extensive ultrasonic treatment allowed the dispersion of the aggregates and the local observation of particles. Fig. 3(a) and (b) present the TEM images of RuSeMo. These particles appear as lumpy material but not fused, their size was well below 100 nm and spherical morphology. TEM images of RuSnMo show that this material had particle size above 100 nm and elongated morphologies (Fig. 3(c) and (d)). It can be proposed that one of the roles of Se is to reduce the particle size. SEM and TEM observations reflect the fractal-like morphology of the RuSeMo and RuSnMo obtained by high energy ball milling. At first glance it seem low possible that ball milling synthesis can produce nanoparticles. Takuya et al. [23] bring examples of how the mechanochemical synthesis (ball milling) can produce nanomaterials well below 100 nm; by selecting suitable chemical reaction paths, stoichiometry of starting materials, milling conditions and post-synthesis treatments. In the present work, the intensive ultrasonic treatment for TEM imaging allow for agglomerate fracture. Similar intensive treatment is performed when the electrocatalyst "ink" for EDR testing is prepared. This forced fracture of particles and the increase of exposed electrocatalyst surface/active sites can be the responsible for the higher exchange current observed at RuSeMo. However, the low electrochemical activity ($j_0 \approx 10^{-6}$ mA cm^{-2}) towards the ORR is correlated to the synthesis method where big agglomerates/particles are formed. The electrochemical activity might be improved by optimization of ball milling conditions and the use of suitable additives to reduce the particle size and produce supported materials.

EDS analysis is collected in Table 1. EDS of RuSeMo reveals low-than expected Mo and Ru content. It was likely a losing of Mo material by the staking at the vials walls. The EDS of RuMoSn is more in agreement with the initial atomic composition 2Ru:1Sn:1Mo. At both materials low-level content of Fe from vial and Zr from balls were present.

SR-PXD patterns are plotted in Fig. 4. The composition obtained by Rietveld refinement of experimental data (MAUD software [24]) is collected in Table 1. Both ball milled materials present the characteristic peaks of metallic Ru (40354-ICSD), confirming the presence of a Ru-rich zone. The refinement of the RuSeMo data indicates the formation of distorted Ru and $RuSe_2$ phases. The distortion of Ru phase in RuSeMo leads to $a = b = 2.724 \pm 0.001$ Å and $c = 4.309 \pm 0.001$ Å; versus the reported Ru (40354-ICSD) $a = b = 2.7508$ Å and $c = 4.2819$ Å. The cell distortion is more evident for the $RuSe_2$. The reported cell size of $RuSe_2$ (24201-ICSD) is $a = b = c = 5.935$ Å, while the refined data reveal $a = b = c = 5.976 \pm 0.003$ Å. Rietveld analysis accounted for less than 1 wt.% Mo as pure phase in the RuSeMo material. The Rietveld weight percentages were used to estimate the atomic percentages (Table 1). The low Mo content follows the EDS atomic composition; differences of the estimated values can be attributed to the presence of amorphous materials and to some extent the formation of a solid solution of Mo in $RuSe_2$.

In the ball milled RuSnMo, it was possible to confirm the formation of Ru_3Sn_7 (54510-ICSD), whereas the peaks of Mo (643962-ICSD) were evident. The lattice distortion of Ru in RuSnMo leads to $a = b = 2.722 \pm 0.001$ Å and $c = 4.304 \pm 0.001$ Å. The Mo in the RuSnMo also presents lattice distortion $a = b = c = 3.161 \pm 0.002$ Å compared to Mo (643962-ICSD) were $a = b = c = 3.147$ Å. The Ru_3Sn_7 also presents a small increase of cell lattice $a = b = c = 9.384 \pm 0.005$ Å compared to the Ru_3Sn_7 (54510-ICSD) $a = b = c = 9.372$ Å. The conclusion is minor atom substitution of Mo in Ru and vice versa, but still

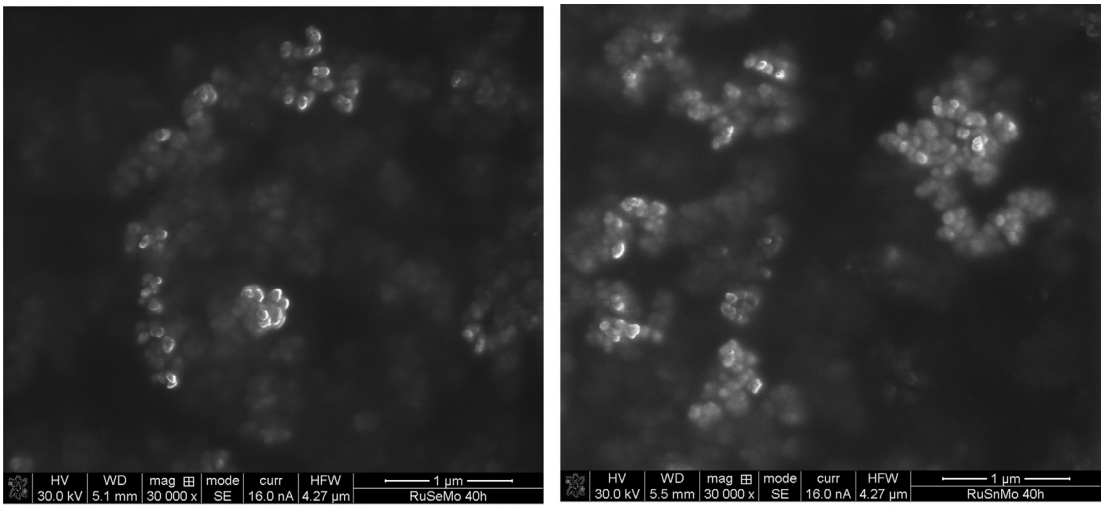

(a) SEM micrograph of ball milled RuSeMo particles. (b) SEM micrograph of ball milled RuSnMo particles.

Fig. 2 – (a) SEM micrograph of ball milled RuSeMo particles. (b) SEM micrograph of ball milled RuSnMo particles.

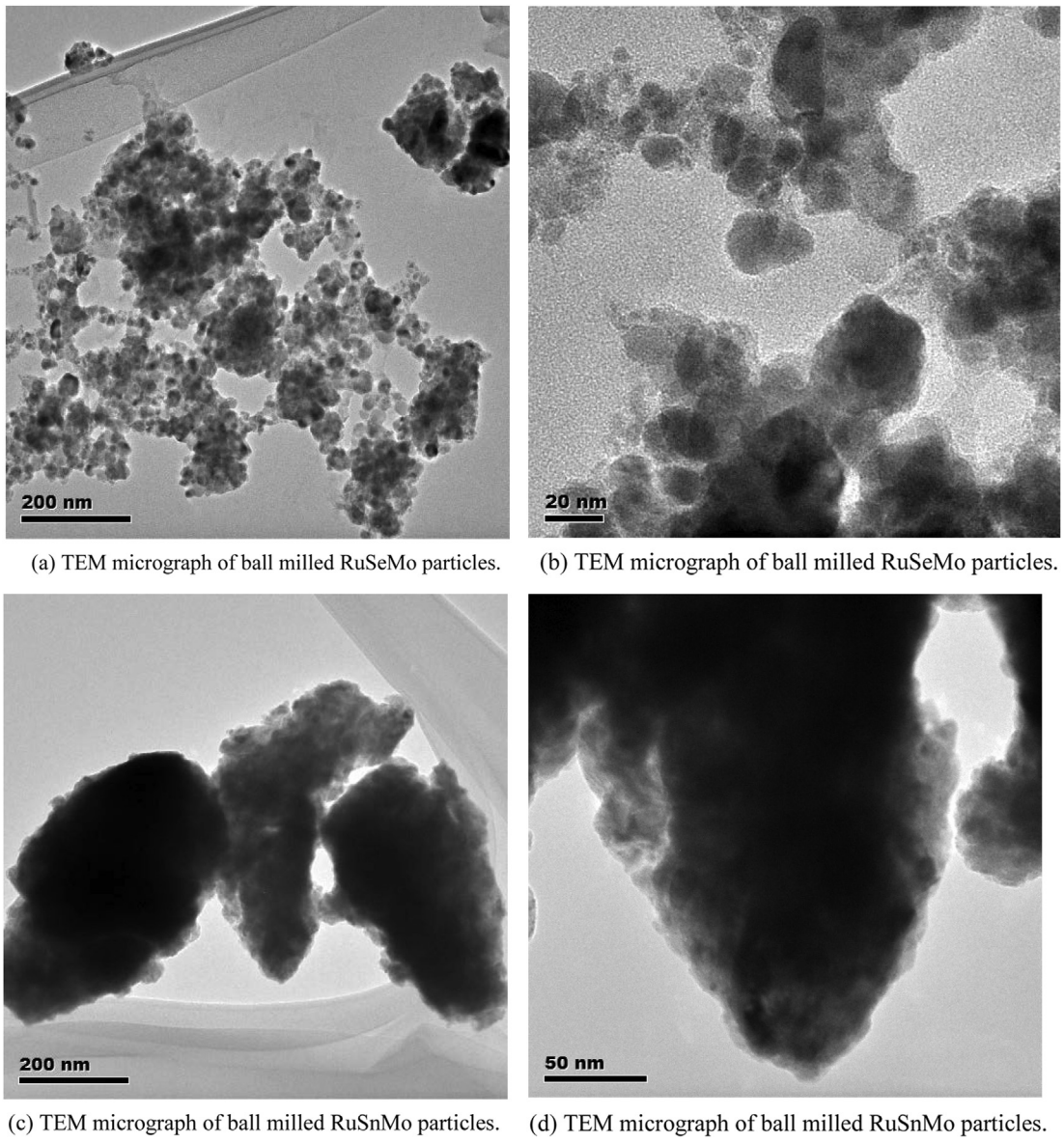

(a) TEM micrograph of ball milled RuSeMo particles. (b) TEM micrograph of ball milled RuSeMo particles.

(c) TEM micrograph of ball milled RuSnMo particles. (d) TEM micrograph of ball milled RuSnMo particles.

Fig. 3 – (a) TEM micrograph of ball milled RuSeMo particles. (b) TEM micrograph of ball milled RuSeMo particles. (c) TEM micrograph of ball milled RuSnMo particles. (d) TEM micrograph of ball milled RuSnMo particles.

conserving Ru and Mo-rich zones at RuSnMo. The distortion in the Ru_3Sn_7 leads to conclude the formation a solid solution of Mo in the Ru_3Sn_7 to some extent.

The ball milling technique can produce materials with ordered and disordered domains. The latter cannot be probed with X-ray diffraction; then X-ray absorption may be a complementary characterization technique. The Fig. 5 shows the Ru L_3 XAS of RuSeMo and RuSnMo normalized to the edge jump. The main characteristics of the Ru L_3-edge XAS spectra are: a sharp peak at 2839.1 eV assigned to $2p_{3/2} \rightarrow 4d_{3/2}$ transition ($E_0 = 2838$ eV), a feature at 2849.3 eV as $2p_{3/2} \rightarrow 5s_{1/2}$ and a feature at 2853.9 eV [25,26]. The general shape of the experimental XAS is in agreement with the metallic ruthenium [27] as the main structure and does not exhibit strong sensitivity to the formation of Ru-phases such as $RuSe_2$ and Ru_3Sn_7. These phases were observed in SR-PXD but did not produce dramatic changes in the whole Ru L_3 XAS. This means that the Ru–Mo; Ru–Se and Ru–Sn interactions are of metallic character mainly. It was expected a noticeable change in the XAS spectra by the $RuSe_2$ formation, however the observations discussed above are in agreement with an XPS and EC-NMR study that demonstrated that the Se, a p-type semiconductor, becomes metallic when interacting with Ru in Ru–Se electrocatalyst due a charge transfer Ru to Se [28]. Small changes near the edge can be observed when the first derivative of the XAS signal is plotted (inset of Fig. 5). The integrated intensity of L_3 peak can be related with the vacancies in the *d*-band [13,29]. The magnitude of the integrated white peak intensity 10 eV below and above of E_0 (and thus 4*d*-vacancies) of RuSeMo is slightly larger than RuSnMo. The

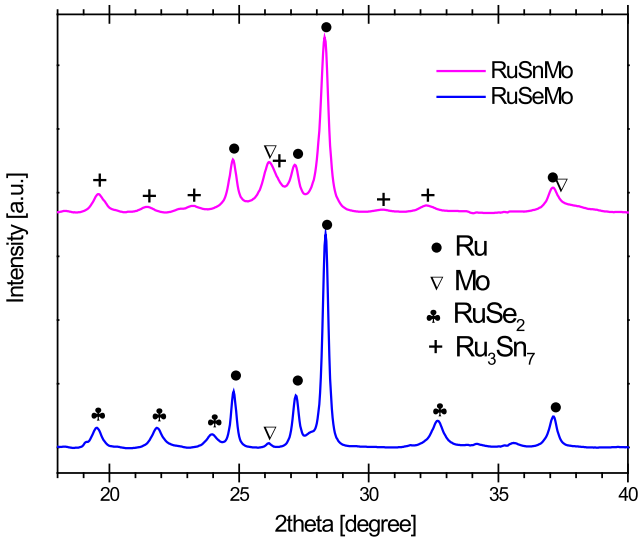

Fig. 4 – Synchrotron powder X-ray diffraction of RuSeMo and RuSnMo particles (λ = 1.0085 A, I711 beamline of MAX-lab laboratory).

$RuSe_2$ formation must increase the Ru 4*d*-vancancies. With slightly less 4*d*-vacancies versus RuSeMo; the RuSnMo can act more effectively as electron reservoir and thus better electron donor during the ORR.

Fig. 6 presents the Mo L_3-edge of RuSeMo and RuSnMo. The experimental spectra display the general shape of the L_3-edged for 4*d* systems where the white L_3 line corresponds to $2p_{3/2}$ to 4*d* transitions [26,27]. The spectrum of ball milled RuSnMo is characteristic of metallic Mo (E_0 = 2520 eV); unlike the ball milled RuSeMo where the L_3-edge is shifted to 2522.9 eV and a splitting of the white line is observed. De Groot et al. have correlated the energy shift to the Mo^{n+} valency; a shift of 3 eV corresponds roughly to Mo^{3+} valency [26]. The splitting depends both on the Mo oxidation state and on the local symmetry at the Mo site [26,30,31]. The splitting indicates a change from pure metallic to cluster-like behavior

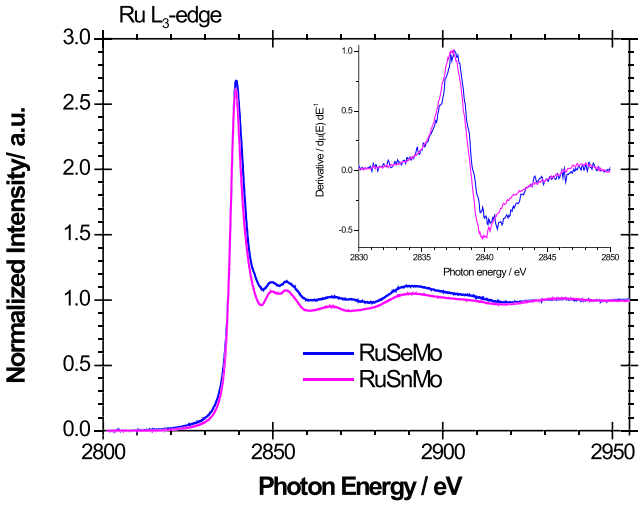

Fig. 5 – Ru L_3-edge X-ray absorption spectra of RuSeMo and RuSnMo. Inset: first derivative at Ru L_3-edge.

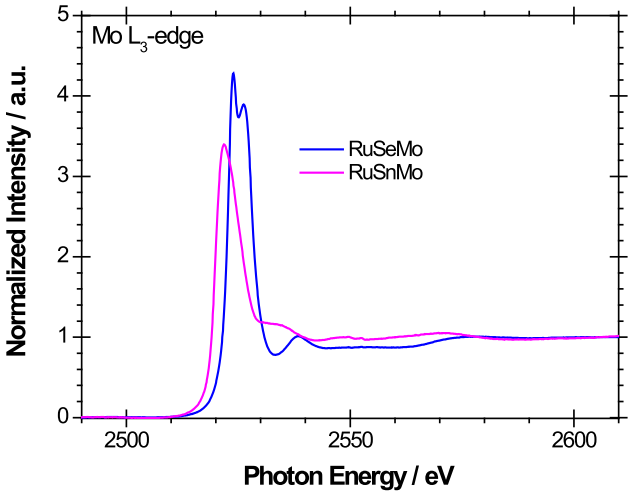

Fig. 6 – Mo L_3-edge X-ray absorption spectra of RuSeMo and RuSnMo.

[26]. The Mo L_3-edge XAS indicates that the Mo–Ru and Mo–Sn are metallic interactions meanwhile the Mo–Se interaction is ionic. Ru and Mo L_3 XAS confirm the SR-PXD data where the Mo in RuSeMo was dissolved into $RuSe_2$ providing a strong Mo–Se interaction. The integrated Mo L_3 white-line peaks lead to the relative ordering in Mo *d*-vacancies RuSeMo > RuSnMo, then the RuSnMo can act more effectively as electron donor during the ORR, justifying the observed preferential $4e^-$ route towards water formation and the well behaved RDE curves.

Despite that the ORR electro–kinetic parameters indicate that the ball milled RuSeMo is better electrocatalyst than ball milled RuSnMo; Ru and Mo L_3-edges indicated that ball milled RuSnMo acts as an electron reservoir and thus good electron donor during the ORR. RuSnMo also present less ohmic losses at high overpotential, the metallic interactions at RuSnMo are more appropriate for a electrocatalyst. Ball milled RuSnMo require further research at fuel cell performance.

Conclusions and perspectives

RuSeMo and RuSnMo particles from ball milling synthesis present electrocatalytic activity towards ORR in acid media. Ball milled RuSnMo is better behaved towards the ORR in acid media.

The low electrochemical activity ($j_0 \approx 10^{-6}$ mA cm^{-2}) towards the ORR is correlated to the synthesis method where big agglomerates/particles are formed. The electrochemical activity might be improved by optimization of ball milling conditions and the use of suitable additives to reduce the particle size and produce supported materials.

The studied particles are composed of Ru-rich and Mo-rich domains, phases such as $RuSe_2$ and Ru_3Sn_7 were also found in RuSeMo and RuSnMo respectively. The formation of distorted Ru, Mo, $RuSe_2$, Ru_3Sn_7 was confirmed by SR-PXD. A change in the valence of Mo was confirmed by Mo L_3 XAS in RuSeMo. Ball milled RuSnMo retains its metallic behavior as observed at Ru and Mo L_3-edge.

Acknowledgments

This project was supported by the Swedish Research Council and the Crafoord Foundation (SEC, KSA). The authors acknowledge the advice of Dr. Stefan Carlson, Dr. Katarina Norén and Dr. Tomás Plivelic during synchrotron data collecting at MAX-lab. KSA acknowledges MAX-lab Synchrotron. KSA acknowledges the CNMN of IPN and to IMP for the support in collecting SEM and TEM images and CONACYT (FOINS 75/2012).

REFERENCES

[1] Schlapbach L. Hydrogen-fuelled vehicles. Nature 2009;460:809–11.
[2] Rabis A, Rodriguez P, Schmidt TJ. Electrocatalysis for polymer electrolyte fuel cells: recent achievements and future challenges. ACS Catal 2012;2:864–90.
[3] Munoz-Flores BM, Kharisov BI, Jimenez-Perez VM, Elizondo Martínez P, Lopez ST. Recent advances in the synthesis and main applications of metallic nanoalloys. Ind Eng Chem Res 2011;50:7705–21.
[4] Feng Y, Gago A, Timperman L, Alonso-Vante N. Chalcogenide metal centers for oxygen reduction reaction: activity and tolerance. Electrochim Acta 2011;56:1009–22.
[5] Suarez-Alcantara K, Rodriguez-Castellanos A, Dante R, Solorza-Feria O. $Ru_xCr_ySe_z$ electrocatalyst for oxygen reduction in a polymer electrolyte membrane fuel cell. J Power Sources 2006;157:114–20.
[6] Suarez-Alcantara K, Solorza-Feria O. Comparative study of oxygen reduction reaction on $Ru_xM_ySe_z$ (M = Cr, Mo, W) electrocatalysts for polymer exchange membrane fuel cell. J Power Sources 2009;192:165–9.
[7] Gonzalez-Huerta RG, Chavez-Carvallar JA, Solorza-Feria O. Electrocatalysis of oxygen reduction on carbon supported Ru-based catalysts in a polymer electrolyte fuel cell. J Power Sources 2006;153:11–7.
[8] Sotelo-Mazón P, González-Huerta RG, Cabañas-Moreno JG, Solorza-Feria O. Mechanically milled Ru_xFe_y electrocatalyst for oxygen reduction in acid media. Int J Electrochem Sci 2007;2:523–33.
[9] Ezeta A, Arce EM, Solorza O, González RG, Dorantes HJ. Effect of the leaching of Ru-Se-Fe and Ru-Mo-Fe obtained by mechanical alloying on electrocatalytical behavior for the oxygen reduction reaction. J Alloys Compd 2009;483:429–31.
[10] Suryanarayana C. Mechanical alloying and milling. Prog Mater Sci 2001;46:1–184.
[11] Zhang DL. Processing of advanced materials using high-energy mechanical milling. Prog Mater Sci 2004;49:537–60.
[12] Manke I, Markötter H, Tötzke C, Kardlilov N, Grothausmann R, Dawson M, et al. Investigation of energy-relevant materials with synchrotron X-rays and neutrons. Adv Eng Mater 2011;13:712–29.
[13] Russell AE, Rose A. X-ray absorption spectroscopy of low temperature fuel cell catalysts. Chem Rev 2004;104:4613–35.
[14] Ezeta-Mejia A, Solorza-Feria O, Dorantes-Rosales HJ, Hallen-Lopez JH, Arce-Estrada EM. Electrocatalytic properties bimetallic surfaces for the oxygen reduction reaction. Int J Electrochem Sci 2012;7:8940–57.
[15] Ezeta-Mejía A, Mora-Hernández JM, Hallen-López JM, Arce-Estrada EM. Exploration of trimetallic nanoparticles as electrocatalysts for oxygen reduction. Int J Electrochem Sci 2013;8:2044–55.
[16] Bard AJ, Faulkner L. Electrochemical methods. 2nd ed. New Jersey: Wiley & Sons; 2001.
[17] Cerenius Y, Ståhl K, Svensson LA, Ursby T, Oskarsson Å, Albertsson J, et al. The crystallography beamline I711 at MAX II. J Synchrotron Radiat 2000;7:203–8.
[18] Hammersley AP, Svensson SO, Hanfland M, Fitch AN, Häusermann D. Two-dimensional detector software: from real detector to idealized image or two-theta scan. High Press Res 1996;14:235–48.
[19] Ravel B, Newville M. ATHENA, ARTEMIS, HEPHAESTUS: data analysis for X-ray absorption spectroscopy using IFEFFIT. J Synchrotron Radiat 2005;12:537–41.
[20] Wang JX, Uribe FA, Springer TE, Zhang J, Adzic RR. Intrinsic kinetic equation for oxygen reduction reaction in acidic media: the double Tafel slope and fuel cell applications. Faraday Discuss 2008;140:347–62.
[21] Suarez-Alcantara K, Solorza-Feria O. Kinetics and PEMFC performance of $Ru_xMo_ySe_z$ nanoparticles as a cathode catalyst. Electrochim Acta 2008;53:4981–9.
[22] Kim J, Lee SM, Srinivasan S, Chamberlin CE. Modeling of proton exchange membrane fuel cell performance with an empirical equation. J Electrochem. Soc 1995;142:2670–4.
[23] Tsuzuki T, McCormick PG. Mechanochemical synthesis of nanoparticles. J Mater Sci 2004;39:5143–6.
[24] Lutterotti L, Bortolotti M, Ischia G, Lonardelli I, Wenk HR. Rietveld texture analysis from diffraction images. Z. Krist Suppl 2007;26:125–30.
[25] Saes M, Bressler C, Abela R, Grolimund D, Johnson SL, Heimann PA, et al. Observing photochemical transients by ultrafast X-ray absorption spectroscopy. Phys Rev Lett 2003;90:047403–4.
[26] de Groot FMF, Hu ZW, Lopez F, Kaindl G, Guillot F, Tronc MJ. Differences between L_3 and L_2 X-ray absorption spectra of transition metal compounds. J Chem Phys 1994;101:6570–6.
[27] Pearson DH, Ahn CC, Fultz B. White lines and d-electron occupancies for the 3d and 4d transition metals. Phys Rev B 1993;47:8471–8.
[28] Babu PK, Lewera A, Chung JH, Hunger R, Jaegermann W, Alonso-Vante N, et al. Selenium becomes metallic in Ru-Se fuel cell catalysts: an EC-NMR and XPS investigation. J Am Chem Soc 2007;129:15140–1.
[29] Mukerjee S, Srinivasan S, Soriaga MP, McBreen J. Effect of preparation conditions of Pt alloys on their electronic, structural, and electrocatalytic activities for oxygen reduction-XRD, XAS, and electrochemical studies. J Phys Chem 1995;99:4577–89.
[30] Bare SR, Mitchell GE, Maj JJ, Vrieland GE, Gland JL. Local site symmetry of dispersed molybdenum oxide catalysts: XANES at the Mo $L_{2,3}$-edges. J Phys Chem 1993;97:6048–53.
[31] Shishido T, Asakura H, Yamazoe S, Teramura K, Tanaka T. Structural analysis of group V, VI, VII metal compounds by XAFS and DFT calculation. J Phys Conf Ser 2009;190:012073–4.